Mon. Not. R. Astron. Soc. **000**, 1–12 (2014) Printed 10 June 2014 (MN LATEX style file v2.2)

Abundance analysis, spectral variability, and search for the presence of a magnetic field in the typical PGa star HD 19400

S. Hubrig[1⋆], F. Castelli[2], J. F. González[3], T. A. Carroll[1], I. Ilyin[1], M. Schöller[4], N. A. Drake[5,6], H. Korhonen[7], M. Briquet[8]

[1] *Leibniz-Institut für Astrophysik Potsdam (AIP), An der Sternwarte 16, 14482 Potsdam, Germany*
[2] *Istituto Nazionale di Astrofisica, Osservatorio Astronomico di Trieste, via Tiepolo 11, 34143 Trieste, Italy*
[3] *Instituto de Ciencias Astronomicas, de la Tierra, y del Espacio (ICATE), 5400 San Juan, Argentina*
[4] *European Southern Observatory, Karl-Schwarzschild-Str. 2, 85748 Garching bei München, Germany*
[5] *Sobolev Astronomical Institute, St. Petersburg State University, Universitetski pr. 28, 198504, St. Petersburg, Russia*
[6] *Observatório Nacional/MCTI, Rua José Cristino 77, CEP 20921-400, São Cristóvão, Rio de Janeiro, RJ, Brazil*
[7] *Finnish Centre for Astronomy with ESO (FINCA), University of Turku, Väisäläntie 20, 21500, Piikkiö, Finland*
[8] *Institut d'Astrophysique et de Géophysique, Université de Liège, Allée du 6 Août 17, Sart-Tilman, Bât. B5C, 4000, Liège, Belgium*

Accepted Received; in original form

ABSTRACT

The aim of this study is to carry out an abundance determination, to search for spectral variability and for the presence of a weak magnetic field in the typical PGa star HD 19400. High-resolution, high signal-to-noise HARPS spectropolarimetric observations of HD 19400 were obtained at three different epochs in 2011 and 2013. For the first time, we present abundances of various elements determined using an ATLAS12 model, including the abundances of a number of elements not analysed by previous studies, such as Ne I, Ga II, and Xe II. Several lines of As II are also present in the spectra of HD 19400. To study the variability, we compared the behaviour of the line profiles of various elements. We report on the first detection of anomalous shapes of line profiles belonging to Mn, and Hg, and the variability of the line profiles belonging to the elements Hg, P, Mn, Fe, and Ga. We suggest that the variability of the line profiles of these elements is caused by their non-uniform surface distribution, similar to the presence of chemical spots detected in HgMn stars. The search for the presence of a magnetic field was carried out using the moment technique and the SVD method. Our measurements of the magnetic field with the moment technique using 22 Mn II lines indicate the potential existence of a weak variable longitudinal magnetic field on the first epoch. The SVD method applied to the Mn II lines indicates $\langle B_z \rangle = -76 \pm 25$ G on the first epoch, and at the same epoch the SVD analysis of the observations using the Fe II lines shows $\langle B_z \rangle = -91 \pm 35$ G. The calculated false alarm probability values, 0.008 and 0.003, respectively, are above the value 10^{-3}, indicating no detection.

Key words: stars: abundances — stars: atmospheres — stars: individual (HD 19400) — stars: magnetic field — stars: chemically peculiar — stars: variables: general

1 INTRODUCTION

A number of chemically peculiar stars with spectral types B7–B9 exhibit in their atmospheres large excesses of P, Mn, Ga, Br, Sr, Y, Zr, Rh, Pd, Xe, Pr, Yb, W, Re, Os, Pt, Au, and Hg, and underabundances of He, Al, Zn, Ni, and Co (e.g., Castelli & Hubrig 2004). These stars are usually called the HgMn stars. The aspect of inhomogeneous distribution of some chemical elements over the surface of HgMn stars was first discussed by Hubrig & Mathys (1995). From a survey of HgMn stars in close spectroscopic binaries, they suggested that some chemical elements might be inhomogeneously distributed on the surface, with, in particular, preferential concentration of Hg along the equator.

⋆ E-mail: shubrig@aip.de

Recent studies revealed that not only Hg, but also many other elements, most typically Ti, Cr, Fe, Mn, Sr, Y, and Pt, are concentrated in spots of diverse size, and different elements exhibit different abundance distributions across the stellar surface (e.g. Hubrig et al. 2006a; Briquet et al. 2010; Makaganiuk et al. 2011a; Korhonen et al. 2013). In SB2 systems, the hemispheres of components facing each other usually display low-abundance element spots, or no spots at all (e.g. Hubrig et al. 2010). Moreover, evolution of the abundance spots of several elements at different time scales was discovered in a few HgMn stars: Briquet et al. (2010) and Korhonen et al. (2013) reported the presence of dynamical spot evolution over a couple of weeks for the SB1 system HD 11753, while Hubrig et al. (2010) detected a secular element evolution in the double-lined eclipsing binary AR Aur.

However, not much is known about the behaviour of different elements in the hotter extension of the HgMn stars, the PGa stars, with rich P II, Mn II, Ga II, and Hg II spectra, and effective temperatures of about 13 500 K and higher (e.g., Alonso et al. 2003; Rachkovskaya et al. 2006).

During our observing run in 2013 July, we obtained a high-resolution, high signal-to-noise (S/N) polarimetric HARPS spectrum of the typical PGa star HD 19400. We downloaded two additional polarimetric spectra of this star, obtained on two consecutive nights in 2011 December, from the ESO archive. These spectra were used to carry out an abundance analysis and to investigate whether HD 19400, similar to HgMn stars, exhibits a weak magnetic field and an inhomogeneous distribution of various elements over the stellar surface. Notably, Maitzen (1984) suggested the presence of a magnetic field in this star using observations of the λ5200 feature. A careful inspection of the spectra acquired on three different epochs revealed the presence of anomalous flat-bottom line profiles belonging to the overabundant elements Hg and Mn (Drake et al. 2013), reminiscent of profile shapes observed in numerous HgMn stars (e.g., Hubrig et al. 2006a, 2011; Makaganiuk et al. 2011a). Moreover, these observations revealed the variability of line profiles belonging to Hg II, Mn II, P II, Fe II, and Ga II. Dommanget & Nys (2002) mention in the CCDM catalogue a nearby component at a separation of 0.″1 and a position angle of 179°. However, no lines belonging to the secondary were detected in the previous spectral studies, indicating that HD 19400 can be treated as a single star. In the following sections, we discuss the results of the abundance determination, the spectral variability detected in the lines of certain elements and our search for the presence of a weak magnetic field.

2 OBSERVATIONS

All three spectropolarimetric observations have been obtained with the HARPS polarimeter (HARPSpol; Snik et al. 2008) attached to ESO's 3.6 m telescope (La Silla, Chile). Two spectropolarimetric observations have been obtained on two consecutive nights on 2011 December 15 and 16, and one on 2013 July 19. The obtained polarimetric observations with a S/N between 500 and 600 in the Stokes I spectra and a resolving power of about $R = 115\,000$ cover the spectral range 3780–6910 Å, with a small gap between 5259 and 5337 Å. Each polarimetric observation consists of several subexposures, obtained with different orientations of the quarter-wave retarder plate relative to the beam splitter of the circular polarimeter. The reduction and calibration of archive spectra was performed using the HARPS data reduction software available at the ESO headquarter in Germany, while the spectra obtained in 2013 July have been reduced using the pipeline available at the 3.6 m telescope in Chile.

Table 1. Logbook of the HARPS polarimetric observations, including the modified Julian date of mid-exposure followed by the achieved signal-to-noise ratio.

MJD	S/N_{4500}
55910.054	820
55911.042	760
56492.327	470

To normalise the HARPS spectra to the continuum level, we used the image of the extracted echelle orders. First, we fit a continuum spline in columns of the image in cross-dispersion direction. Each column is fitted in a number of subsequent iterations until it converges to the same upper envelope of the continuum level. After each iteration, we analyze the residuals of the fit and make a robust estimation of the noise level based upon a statistical test of the symmetric part of the distribution. All pixels whose residuals are below the specified sigma clipping level are masked out from the subsequent fit. This way the smooth spline function is rejecting all spectral lines below, but leaving the continuum pixels to fit. Once all columns are processed, we fit the resulting smoothed curves in the dispersion direction by using the same approach with the robust noise estimation from the residuals, but this time rejecting possible outliers above and below the specified sigma clipping level. As a result, we create a bound surface with continuous first derivatives in the columns and rows. We employ a smoothing spline with adaptive optimal regularisation parameters, which selects the minimum of the curvature integral of the smoothing spline. As a test for the validity of the continuum fit, we check whether the normalised overlapping echelle orders are in good agreement with each other. The same is applied to the very broad hydrogen lines, whose wings may span over two or even three spectral orders. The typical mismatch between the red and blue ends of the neighboring orders is well within the statistical noise of these orders. The usual procedure to normalise a series of polarimetric observations of the same target, but with different angles of the retarder, is to create a sum of the individual observations, normalise it to the continuum in the way described above, and to use the master normalised image as a template for the individual observations: by taking the ratio and fitting a regular spline to it, which then finally defines the continuum surface for the individual observations.

The Stokes I and V parameters were derived following the ratio method described by Donati et al. (1997), and null polarisation spectra were calculated by combining the subexposures in such a way that polarisation cancels out. These steps ensure that no spurious signals are present in the obtained data (e.g. Ilyin 2012). The observing logbook is presented in Table 1, where the first column gives the date of observation, followed by the S/N ratio per resolu-

tion element of the spectra in the wavelength region around 4500 Å.

3 MODEL PARAMETERS AND ABUNDANCES OF HD 19400

The starting model parameters of HD 19400 were derived from Strömgren photometry. The observed colors $(b-y) = -0.066$, $m_1 = 0.111$, $c_1 = 0.512$, $\beta = 2.708$ were taken from the Hauck & Mermilliod (1998) Catalogue[1]. The synthetic colors were taken from the grid computed for [M/H] = 0 and microturbulent velocity $\xi = 0\,\mathrm{km\,sec^{-1}}$ (Castelli & Kurucz 2003; Castelli & Kurucz 2006)[2]. Zero reddening was adopted for this star, in agreement with the results from the UVBYLIST code of Moon (1985). Observed c_1 and β indices were reproduced by synthetic indices for model parameters $T_{\rm eff} = 13\,868 \pm 150$ K and $\log g = 3.81 \pm 0.06$, where the errors are associated with estimated errors of ± 0.015 mag and ± 0.005 mag for the observed c_1 and β indices, respectively.

The parameters from the photometry were adopted for computing an ATLAS9 model with solar abundances for all the elements and zero microturbulent velocity. Using the WIDTH code (Kurucz 2005), we derived Fe II and Fe III abundances from the equivalent widths of 34 Fe II and four Fe III lines. The equivalent widths were measured with the SPLOT task of the IRAF package using the "e" option, which integrates the intensity over the line profile. No Fe I equivalent widths were measured because the observed lines are weak and blended. The Fe II and Fe III abundances both satisfied the ionisation equilibrium condition and provided a good agreement between most of the observed and computed blended Fe I weak profiles. We did not find any trend of Fe II abundances with the excitation potential, indicating that the adopted temperature is correct. We also did not find any trend of Fe II abundances with equivalent widths, indicating that also the assumption of zero microturbulent velocity is correct. For solar abundances, the model was also able to reproduce the Balmer lines, indicating that the adopted gravity is correct.

The ATLAS9 model was used to derive the abundance for all those elements that show lines in the spectrum. Whenever possible, equivalent widths were measured. For weak and blended lines and for lines that are blends of transitions belonging to the same multiplet, such as Mg II 4481 Å, He I lines, and most O I lines, we derived the abundance from the line profiles. The synthetic spectrum was also used to determine upper abundance limits from those lines predicted for solar abundances, but not observed.

The SYNTHE code (Kurucz 2005), together with line lists based mostly on Kurucz's data (Castelli & Hubrig 2004; Castelli & Kurucz 2010; Kurucz 2011; Yüce et al. 2011) and including also data taken from the NIST database (version 5)[3] were used to compute the synthetic spectrum. The synthetic spectrum was broadened both for a Gauss profile corresponding to the 115 000 resolving power of the HARPS instrument and for a rotational velocity $v \sin i = 32\,\mathrm{km\,s^{-1}}$. This value was derived from the comparison of the observed and computed profile of several lines. We estimate an uncertainty of the order of $0.5\,\mathrm{km\,s^{-1}}$ for this choice.

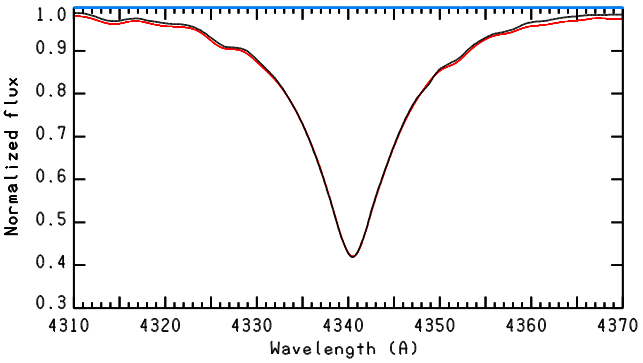

Figure 1. Comparison of the H_γ profile observed in the low-resolution FORS 1 spectrum (black) with that computed using the ATLAS12 model with parameters $T_{\rm eff} = 13\,500$ K and $\log g = 3.9$ (red in the online version).

Once all abundances were determined in this way, we computed an ATLAS12 model (Kurucz 2005) for the individual abundances having the same parameters as for the ATLAS9 model. However, the new ATLAS12 model did not reproduce neither the Fe II-Fe III equilibrium nor the hydrogen lines. In fact, the non-solar abundances of several elements, and in particular the helium underabundance, altered the model structure in a consistent way. We therefore searched for the ATLAS12 model adequate to assure the Fe II-Fe III ionisation equilibrium and the Balmer lines reproducibility. We found that the ATLAS12 model with parameters $T_{\rm eff} = 13\,500$ K and $\log g = 3.9$ met these requirements. The comparison between the computed H_γ profile and the H_γ profile observed in the FORS 1 spectrum at a resolution of ∼2000 on 2003 August 1 (ESO Prg. 71.D-0308(A)) is presented in Fig. 1.

The abundances $\log(N_{\rm elem}/N_{\rm tot})$ of HD 19400 derived from the ATLAS12 model either from equivalent widths or line profiles are listed in Table 2, together with the solar abundances taken from Asplund et al. (2009). Similar to previous spectroscopical studies of HD 19400, no lines belonging to the secondary were detected in the three HARPS spectra. All the lines and atomic data used for the abundance analysis are listed in Table A1.

The most overabundant element is Xe ([+5.22]), followed by Hg ([+4.75]), Ga ([+3.97]), P ([+2.24]), Mn ([+1.71]), Fe [(+0.73)], and Ti ([+0.67]). The elements Ne, Si, Ca, and Cr are marginally overabundant. We note that a nearly solar abundance of −4.45 dex, rather than the average value of −4.37 dex derived from the equivalent widths, better reproduces with the synthetic spectrum most of the observed Si lines.

Helium is underabundant (∼ [−1.1]), but it is difficult to state a definite abundance value, because some observed profiles cannot be fitted by the computed ones, whichever is the adopted abundance. These are the lines at 4026, 4387, 4471, and 4921 Å. We assumed an average abundance of $N(He)/N_{\rm tot} = 0.007$, which reproduces rather well most of the lines listed in Table A1. The wings of the lines at 4026, 4471, 5075, and 6678 Å are rather well reproduced by an average abundance of −2.17 dex derived from all the He I lines, but the observed core is weaker than the computed

[1] http://obswww.unige.ch/gcpd/gcpd.html
[2] http://wwwuser.oat.ts.astro.it/castelli/colors/uvbybeta.html
[3] http://www.nist.gov/pml/data/asd.cfm

Table 2. Abundances $\log(N_{elem}/N_{tot})$ for HD 19400. For each element listed in the first column, we present the abundance computed using the ATLAS12 model in the second column. In parentheses is the number of lines adopted to derive the abundance for a given ion. Blended lines were counted only once. In the third column, we list the deviations from solar abundances (Asplund et al. 2009) presented in column 4. The last column gives the abundances derived by Alonso et al. (2003).

Element	HD 19400 [13500 K,3.9,ATLAS12]	Star-Sun	Sun	Alonso et al. (2003) [13350 K,3.76,ATLAS9]
He I	−2.17±0.08: (14)	[−1.11]:	−1.05	−1.52
C II	−4.12±0.02 (4)	[−0.51]	−3.61	−3.52±0.28
O I	−3.90 (2)	[−0.55]	−3.35	−3.31±0.07
Ne I	−3.77±0.07 (6)	[+0.34]	−4.11	
Na I	−5.71 (2)	[+0.09]	−5.80	
Mg II	−5.06 (4)	[−0.62]	−4.44	−4.65±0.30
Al II	⩽−6.77 (2)	⩽[−1.18]	−5.59	
Si II	−4.36±0.17 (10)	[−0.17]	−4.53	−4.28±0.31
Si III	−4.37±0.02 (2)	[−0.16]	−4.53	
P II	−4.26±0.15 (33)	[+2.28]	−6.63	−5.95±0.16
P III	−4.44±0.09 (4)	[+2.19]	−6.63	
S II	−5.82 (1)	[−0.90]	−4.90	−5.07±0.47
Ca II	−5.50: (1)	[+0.20]:	−5.70	
Ti II	−6.35±0.07 (9)	[+0.74]	−7.09	−5.69±0.37
Cr II	−6.24±0.09 (5)	[+0.16]	−6.40	−5.45±0.42
Mn II	−4.94±0.18 (6)	[+1.67]	−6.61	−4.57±0.33
Fe II	−3.79±0.14 (35)	[+0.75]	−4.54	−3.75±0.31
Fe III	−3.82±0.10 (4)	[+0.72]	−4.54	−3.67±0.30
Ni II	−5.84 (1)	[−0.02]	−5.82	−5.51±0.34
Ga II	−5.19±0.17 (12)	[+3.81]	−9.00	
Sr II	−9.07 (1)	[+0.10]	−9.17	−6.95±0.38
Xe II	−4.65±0.17 (6)	[+5.15]	−9.80	
Hg II	−6.16±0.13 (3)	[+4.71]	−10.87	−4.43

Table 3. Line by line abundances of HD 19400 from the ATLAS12 model with parameters $T_{\rm eff} = 13\,500$ K, $\log g = 3.9$. In the second and third columns, we give the oscillator strength with the corresponding data base source. The low excitation potential is listed in column 4, followed by the equivalent width and the derived abundance. For a number of lines, the abundance was derived from line profiles. The full table is available online.

HD 19400[13500,3.9,ATLAS12]						
λ(Å)	log gf	Ref.[a]	χ_{low}	W(mÅ)	$\log(N_{elem}/N_{tot})$	Remarks
$\log(N(\text{He I})/N_{tot}) = -2.17 \pm 0.08$:						
3867.4723	−2.038	NIST5	169086.766	profile	−2.155	
3867.4837	−2.260	NIST5	169086.843	profile	−2.155	
3867.6315	−2.737	NIST5	169087.631	profile	−2.155	
4009.2565	−1.447	NIST5	171134.897	profile	−2.155	
4026.1844	−2.628	NIST5	169086.766	profile	−2.155::	no fit
4026.1859	−1.453	NIST5	169086.766	profile	−2.155::	
4026.1860	−0.704	NIST5	169086.766	profile	−2.155::	
4026.1968	−1.453	NIST5	169086.843	profile	−2.155::	
4026.1983	−0.976	NIST5	169086.843	profile	−2.155::	

one. This kind of behaviour, common to several HgMn stars (e.g. Castelli & Hubrig 2004), is ascribed to vertical abundance stratification. The whole line at 4388 Å and the red wing of the line at 4922 Å can not be fitted. The cause could be due to the several blends affecting them. The other He I lines at 3867, 4009, 4121, 4713, 5015, and 5047 are well reproduced by the −2.17 dex abundance. Some of them have minor contributions of blends.

Other underabundant elements are Al (⩽[−1.2]), S ([−1.1]), O ([−0.69]), C ([−0.60]), and Mg ([−0.60]). Finally, Ni is marginally underabundant.

We could identify a few observed but not predicted lines as As II. In fact, no As II lines are included in our line list owing to the lack of log gf values and excitation potentials for them. We used As II wavelengths listed in the NIST database to identify the lines observed at 4494.30, 5497.727, 5558.09, 5651.32, and 6170.27 Å as due to As II. Arsenic was report-

edly also present in the HgMn stars 46 Aql (Sadakane et al. 2001) and HD 71066 (Yüce et al. 2011).

No lines of rare earth elements, as well as no lines of Y II, Pt II, and Au II were observed.

For comparison, the abundances from Alonso et al. (2003) are listed in the last column of Table 2. There is a large disagreement for almost all elements, except for silicon and iron. The differences in the abundances for iron and silicon amount to 0.05 dex for Fe II, 0.15 dex for Fe III, and 0.06 dex for Si II. They can be related with both the different ATLAS9 parameters and the microturbulent velocities adopted for the abundance analysis. The ATLAS9 parameters in this study are $T_{\rm eff} = 13\,870$ K, $\log g = 3.8$, [M/H] = 0.0, while those of Alonso et al. (2003) are $T_{\rm eff} = 13\,350$ K, $\log g = 3.76$, [M/H] = 0.5; the microturbulent velocities are $\xi = 0.0\,{\rm km\,sec^{-1}}$ and $1.2\,{\rm km\,sec^{-1}}$, respectively. However, the differences for all the other elements are too large to be only due to the different choices for the parameters. Furthermore, Alonso et al. (2003) derived abundances for numerous elements that we did not observe at all in our spectra, while we identified and derived abundances for Ne I, Ga II, and Xe II that were not mentioned at all by Alonso et al. (2003), although these elements are present with numerous lines. Unfortunately, they did not publish the list of lines and equivalent widths they used, so that any further comparison is not possible.

The ATLAS12 model was preferred to ATLAS9 for final abundance determination, to ensure consistency with the SYNTHE code in computing the line profiles; however abundance values derived using ATLAS9 and ATLAS12 differ by no more than 0.05 dex. The observed and synthetic spectra are presented on F. Castelli's web page[4] together with the line-by-line identification.

3.1 Emission lines

Similar to the spectral behaviour of a number of HgMn stars, the lines of multiplet 13 of Mn II ($\lambda\lambda$ 6122-6132 Å) appear to be affected by emission. In fact, a very weak emission is observed for the blends $\lambda\lambda$ 6125.861, 6126.225 Å, while a well observable strong absorption is predicted at these wavelengths. Furthermore, the blends at $\lambda\lambda$ 6122.432, 6122.807 Å, at 6128.726, 6129.019, 6129.237 Å, and at 6130.793, 6131.011, 6131.918 Å are observed much weaker than computed, so that the core could have been filled by emission.

Other CP stars showing this kind of emission are, for example, 3 Centauri A (Sigut et al. 2000), (Wahlgren & Hubrig 2004), 46 Aquilae (Sigut et al. 2000), HR 6000 (Castelli & Hubrig 2007), and HD 71066 (Yüce et al. 2011). This phenomenon was explained either in the context of non-LTE line formation (Sigut 2001) or as due to a possible fluorescence mechanism (Wahlgren & Hubrig 2000).

3.2 Anomalous line profile shapes

In all HARPS spectra the lines of Mn II and Hg II present anomalous flat-bottom line profiles reminiscent of profile shapes observed in numerous HgMn stars (e.g., Hubrig et al. 2006a, 2011; Makaganiuk et al. 2011a), while the lines of other elements exhibit typical rotationally broadened line profiles. As an example, we display in Fig. 2 the average Mn II profile overplotted with the average Fe II profile, using the best almost blend-free lines of moderate strength. To construct the average Mn II profile, we employed the Mn II lines $\lambda\lambda$4292.2, 4363.3, 4478.6, 4518.9, 4738.3, 4755.7, and 4764.7. Three of them, $\lambda\lambda$4738.3, 4755.7, and 4764.7, have not been used in the abundance analysis because of their unknown hyperfine structure. We note that two more Mn II lines, $\lambda\lambda$4206.4 and 4365.2, were employed in the abundance analysis (see Table A1). They are not included in our sample of lines selected for the search of variability, as the line at $\lambda\lambda$4206.4 is slightly disturbed by a blend in the blue wing and the weak line at $\lambda\lambda$4365.2 is considerably affected by noise at the third epoch. In the calculation of the average Fe II profile, we used the Fe II lines $\lambda\lambda$4122.7, 4296.6, 4491.4, 4522.6, 4923.9, 5002.0, and 5061.7, which constitute a subset of the sample of Fe II lines employed in the Fe abundance determination.

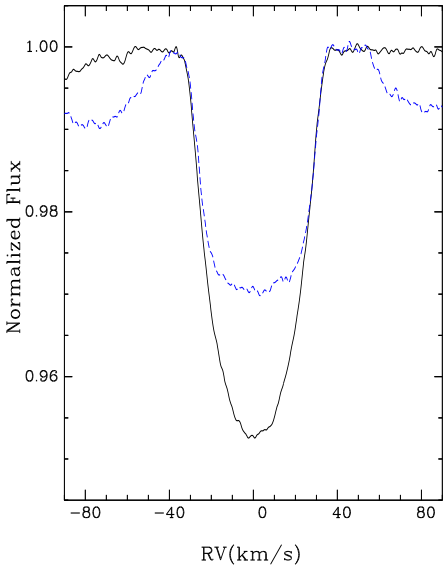

Figure 2. Comparison of the average Mn II line profile (dashed line) with the average Fe II line profile (solid line).

The calculation of the synthetic spectrum for individual Mn II and Hg II lines indicates that the anomalous flat-bottom line profile shape is not caused by the presence of isotopic/hyperfine structure. In the top panel of Fig. 3, we display the synthetic profile of the Hg II λ3984 line overplotted with the observed line profile. The bottom panel presents the synthetic and observed profiles of the Mn II λ4478 line. The observed anomalous profile shape of both lines is reminiscent of the behaviour of line profiles of various elements in typical HgMn stars (e.g. Hubrig et al. 2006a). In spectroscopic binaries these elements are frequently concentrated in non-uniform equatorial bands, which disappear exactly on the surface area, which is permanently facing the secondary (e.g. Hubrig et al. 2010).

[4] http://wwwuser.oats.inaf.it/castelli/hd19400/hd19400.html

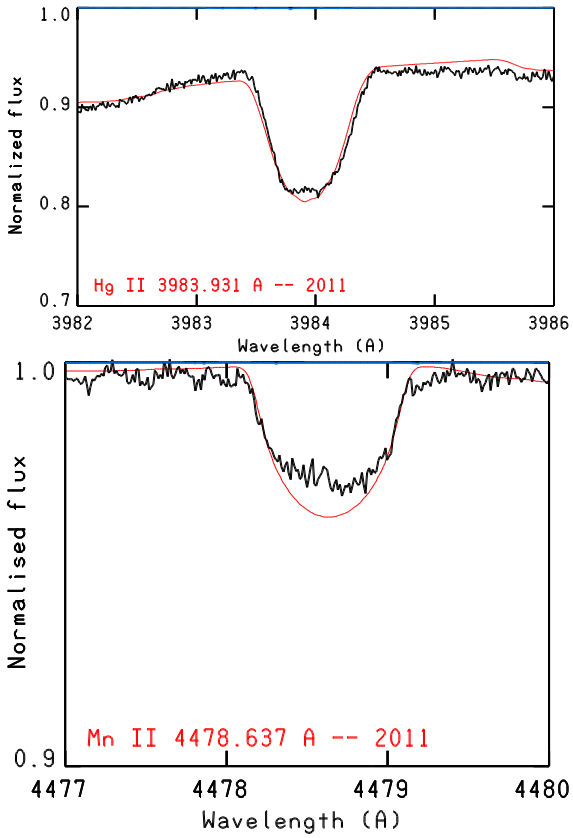

Figure 3. Hg II and Mn II line profiles observed in the HARPSpol spectrum obtained in 2011 highlighted in black together with the synthetic profile shown by the thin red line. The shape of the line profiles belonging to Hg II and Mn II deviates from the purely rotationally broadened profiles observed in the Fe II and Cr II lines, indicating an inhomogeneous distribution of Hg and Mn on the stellar surface.

4 SPECTRAL VARIABILITY

For the study of the spectral variability we have on our disposal two HARPS spectra taken on two consecutive nights in 2011 December, while the third HARPS spectrum was obtained in 2013 July. The spectra have different quality with a S/N of about 800 for observations in 2011 and a S/N of only about 500 for the observation in 2013. To better understand the chemical spot pattern on the surface of HD 19400, we decided to analyse the spectral variability by comparison of observations separated by two timescales. On the one hand we compared the spectra from 2011 with each other to study the day-to-day variations, and on the other hand, we compared the spectrum obtained in 2013 against the average of the two spectra from 2011 to search for long term variation in the line profiles.

In the left panel of Fig. 4, we compare the mean Mn II profiles obtained on two nights in 2011. In the difference spectrum the rms of the noise in the nearby continuum is about 0.05% while the variations are about 0.15%. The variability of the Mn lines is detected therefore at a level of 3σ. We note that if the high-frequency noise is filtered, it becomes evident that the observed day-to-day variation is in fact four times larger than the σ of the noise of similar frequency. The year-to-year variations are apparently not

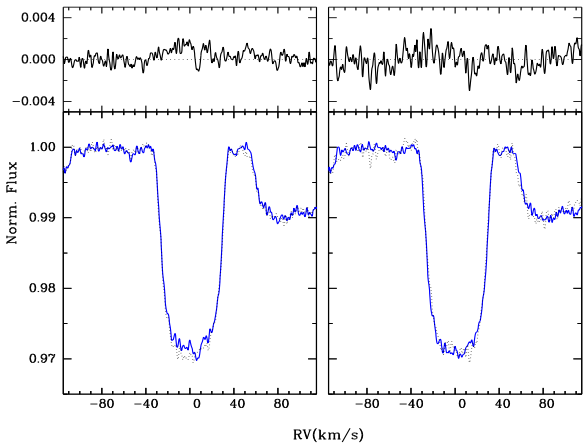

Figure 4. Profile variations of the Mn lines. Left panel: day-to-day variations; solid and dotted lines correspond to 2011 December 15 and 16, respectively. Right panel: year-to-year variations; solid and dotted lines present 2011 and 2013 observations, respectively. The upper part of each panel shows the difference between the two plotted spectra.

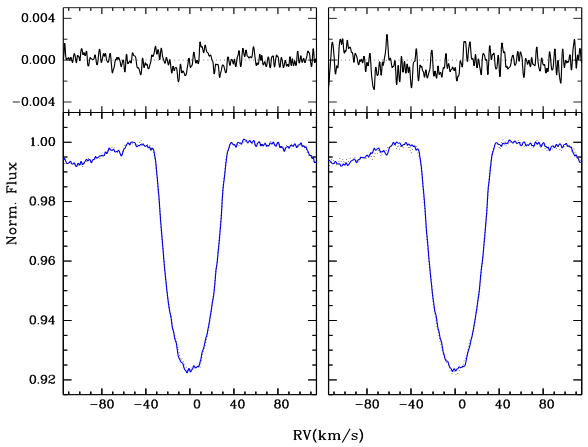

Figure 5. Profile variations of the Fe lines. Left panel: day-to-day variations; solid and dotted lines correspond to 2011 December 15 and 16, respectively. Right panel: year-to-year variations; solid and dotted present 2011 and 2013 observations, respectively. The upper part of each panel shows the difference between the two plotted spectra.

larger than the day-to-day variations, and, since the S/N of the spectrum obtained in 2013 is lower, the variations between 2011 and 2013 are not so clear. The flux differences, however, are still present at a level of about 2σ.

The same procedure as for the study of the Mn lines was applied to the Fe lines. Figure 5 shows the mean profile of the seven Fe lines. The day-to-day flux variations within the line profile are on the order of 0.13%, which is 3 times larger than the noise and of the order of 4σ, if high frequencies are filtered. Year-to-year flux differences are similar in size, but in this case represent only a level of about 1.5 times over the noise and $\sim 2\sigma$, after filtering high frequencies.

To study the variability of the P II lines, we selected the following six blend-free P II lines: $\lambda\lambda$4420.71, 4530.82, 4589.85, 5386.90, 6024.18, and 6043.08. The line profile difference between the two spectra taken in 2011 resembles

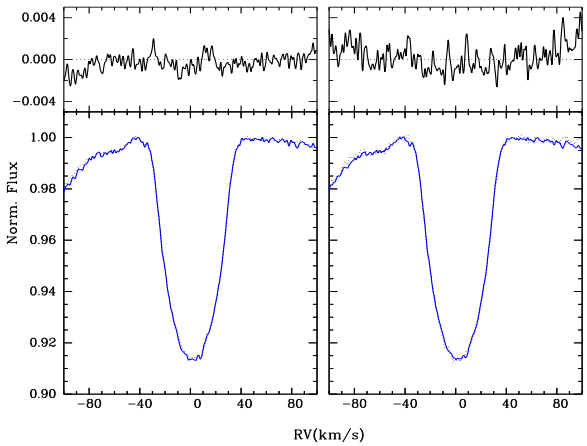

Figure 6. Profile variations of the P lines. Left panel: day-to-day variations; solid and dotted lines correspond to 2011 December 15 and 16, respectively. Right panel: year-to-year variations; solid and dotted lines present 2011 and 2013 observations, respectively. The upper part of each panel shows the difference between the two plotted spectra.

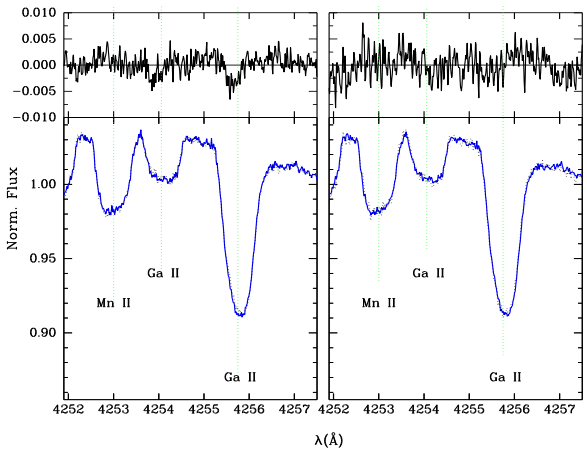

Figure 7. Profile variations of the Ga lines. Left panel: day-to-day variations; solid and dotted lines correspond to 2011 December 15 and 16, respectively. Right panel: year-to-year variations; solid and dotted lines present 2011 and 2013 observations, respectively. The upper part of each panel shows the difference between the two plotted spectra.

that of the Fe lines (Fig. 6). However, the noise in this case is higher and the detection would be only at a level of 2σ. The year-to-year comparison shows no significant variation, probably due to the rather high noise level.

The behaviour of line profiles belonging to other elements with strong overabundances, in particular Hg and Ga, also indicates a non-uniform distribution. Unfortunately, for these elements, the number of useful lines is low and consequently the detection threshold is higher. Figure 7 shows the differences between the spectra around the only two clean Ga lines: λ4254.0 and λ4255.7. We note that the shape difference in the line profiles between spectra obtained on 2011 December 15 and 16 is the same for both Ga lines. This supports the genuineness of the variation behaviour, even if the flux differences are not larger than 2σ. The differences with respect to the 2013 spectrum are within the noise level.

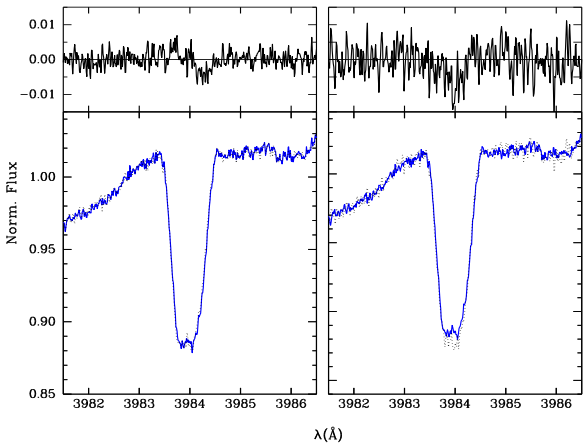

Figure 8. Profile variations of the Hg line. Left panel: day-to-day variations; solid and dotted lines correspond to 2011 December 15 and 16, respectively. Right panel: year-to-year variations; solid and dotted lines present 2011 and 2013 observations, respectively. The upper part of each panel shows the difference between the two plotted spectra.

It is a remarkable finding that the Ga II lines appear indicative of variability. Previous studies of He-weak magnetic Bp stars with similar atmospheric parameters and with well established strong magnetic fields also indicated strong overabundances of P, Ga, Xe, and a few heavy elements, such as Pt and Hg (e.g. Collado & Lopez-Garcia 2009). Furthermore, a number of magnetic Bp stars with strongly overabundant Ga display a large variation of Ga lines, which become the strongest at longitudinal magnetic field maxima, suggesting that Ga is accumulating near the magnetic poles (e.g. Artru & Freire-Ferrero 1988). Interestingly, Alecian & Artru (1987) presented the radiative accelerations of gallium in Bp star atmospheres and concluded that the presence of a magnetic field strongly modifies the gallium accumulation.

Also the Hg line at 3984 Å presents noticeable variations (Fig. 8). Day-to-day variations are of the order of 0.4%, while differences of about 0.8% are present between the 2011 and 2013 observations. In both cases the variation is at a 2σ level. If high-frequencies are filtered, then the variations are at a $3-4\sigma$ level.

Due to the small number of available spectra, it is currently not possible to decide whether the variability pattern of the line profiles belonging to different elements can be explained by an inhomogeneous element distribution on the stellar surface, or is due to pulsations. Although no information on the rotational period is given in the literature, its upper limit can be estimated from the measured $v \sin i$-value and the stellar radius. Using $v \sin i = 32.0 \pm 0.5$ km s^{-1} and $R = 3.7 \pm 0.5\,R_\odot$ calculated using main-sequence evolutionary CLÉS models (Scuflaire et al. 2008), we obtain an upper limit of $P \leqslant 5.85 \pm 0.8$ days. It is clear that with such a rather low value for the rotation period, one can already expect to see weak variability in observations obtained on two consecutive nights.

In Fig. 9 we show the position of HD 19400 in the $\log T_{\rm eff}$–$\log g$ diagram. together with the boundaries of the theoretical instability strips calculated for different metallicities ($Z = 0.01$ and $Z = 0.02$) and using the OP opac-

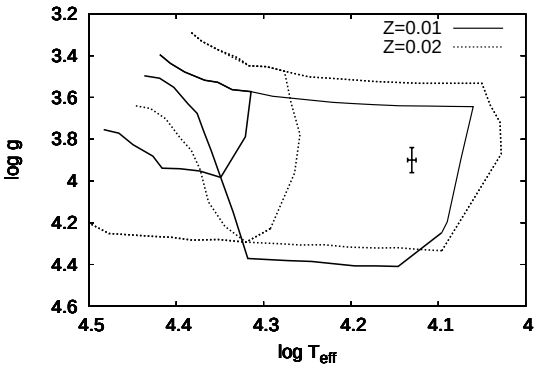

Figure 9. The position of the PGa star HD 19400 in the H-R diagram. The boundaries of the theoretical instability strips for β Cep and SPB stars are taken from Miglio et al. (2007) for OP opacities. Full lines correspond to strips for metallicity $Z = 0.01$ and dotted lines to strips with metallicity $Z = 0.02$.

Table 4. Previous magnetic field measurements of HD 19400 using FORS 1/2. In the first column, we list the modified Julian date of mid-exposure followed by the measurements of the mean longitudinal magnetic field $\langle B_z \rangle_{\rm all}$ using all available spectral lines and $\langle B_z \rangle_{\rm hyd}$ using only hydrogen lines. All quoted errors are 1σ uncertainties.

MJD	$\langle B_z \rangle_{\rm all}$ [G]	$\langle B_z \rangle_{\rm hyd}$ [G]
52852.371	151±46	217±65
55845.295	14±24	32±26
55935.109	−65±26	−110±30

ities (http://cdsweb.u-strasbg.fr/topbase/op.html, see also Miglio et al. 2007). The PGa star HD 19400 with $T_{\rm eff}$ = 13 500 K and log $g = 3.90$ falls well inside the classical instability strip, where slowly pulsating B-type (SPB) stars are found with expected pulsation periods from several hours to a few days. Also classical magnetic Bp stars are located in the same region of the H-R diagram and frequently display strong overabundances of P, Ga, Xe, and heavy elements.

Since polarimetric observations usually consist of a number of short sub-exposures taken at different angles of the retarder wave plate, we used all available Stokes I spectra for each sub-exposure to search for the presence of short-term variations in Mn and Hg line profiles. During both nights in 2011 December, the time difference between individual subexposures accounts for 13 min, while it is about 20 min for the observations in 2013 July. In Fig. 10, we present the behaviour of line profiles of the Hg II λ3984 line, and the Mn II λ4478 line, in HARPSpol subexposures obtained on 2011 December 15 and 16 and on 2013 July 19. No notable line profile variations above the noise level, which is about 0.22% of the continuum flux in the 2011 spectra and about 0.32% in 2013, are detected on these time scale.

5 MAGNETIC FIELD

A few polarimetric spectra of HD 19400 were previously obtained with FORS 1 (Hubrig et al. 2006b), and most recently with FORS 2 on Antu (UT1) from 2011 May to 2012 January (Hubrig et al. 2012) at the rather low resolution of ∼2000. The magnetic field measurements from these earlier data are presented in Table 4 together with the modified Julian date of mid-exposure. Out of the three measurements, weak magnetic field detections at a 3σ significance level were achieved on two different epochs. Given the low resolution of FORS 1/2, these spectra do not allow however to measure the longitudinal magnetic field on lines of individual elements separately.

Table 5. Shifts between the line centres of gravity in the right and left circularly polarised spectra obtained on three different nights. In the first column, we list the wavelengths of the Mn II lines followed by their corresponding Landé factors and the wavelength shifts in Å on each epoch.

λ [Å]	$g_{\rm eff}$	$\Delta\lambda$ [Å] Night 1	Night 2	Night 3
4000.033	1.076		0.0001	0.0014
4110.615	1.002	−0.0010	0.0004	
4184.454	1.065	−0.0024	−0.0005	
4206.367	1.362	−0.0001	0.0020	−0.0013
4240.390	0.929	−0.0046	0.0040	0.0024
4259.200	1.315	−0.0009	−0.0016	−0.0013
4260.467	2.725	−0.0027	0.0040	0.0086
4292.237	1.270	−0.0001		0.0051
4326.639	1.379	−0.0013	0.0004	0.0011
4363.255	1.112	−0.0019	−0.0005	0.0043
4365.217	1.500		−0.0042	0.0067
4478.637	1.500	−0.0104	0.0026	
4518.956	1.507	−0.0007	−0.0013	
4727.841	0.506		0.0031	0.0029
4730.395	0.712	0.0022	−0.0022	
4734.136	0.724	−0.0010		
4738.290	1.080	0.0005		
4755.727	1.058	−0.0029	0.0009	
4764.728	1.027	−0.0009	0.0019	0.0032
4791.782	1.085	−0.0076	−0.0042	−0.0030
4806.823	1.048	0.0013	0.0028	
4839.737	1.358	−0.0031	−0.0027	0.0090

We note that the magnetic field topology in HgMn stars is currently unknown. The recent study of Hubrig et al. (2012) seems to indicate the existence of intriguing correlations between the strength of the magnetic field, abundance anomalies, and binary properties. Measurement results for a few stars revealed that element underabundance (respectively overabundance) is observed where the polarity of the magnetic field is negative (respectively positive). An inhomogeneous chemical abundance distribution is observed most frequently on the surface of upper-main sequence Ap/Bp stars with large-scale organised magnetic fields. The abundance distribution of certain elements in these stars is usually non-uniform and non-symmetric with respect to the rotation axis, but shows a kind of symmetry between the topology of the magnetic field and the element distribution. Assuming that a similar kind of symmetry exists in HgMn and PGa stars, it appears reasonable to use the Mn II lines for magnetic field measurements since Mn II shows the strongest variability in the spectra of HD 19400.

The major problem in the analysis of high-resolution spectra is the proper line identification of blend free spectral

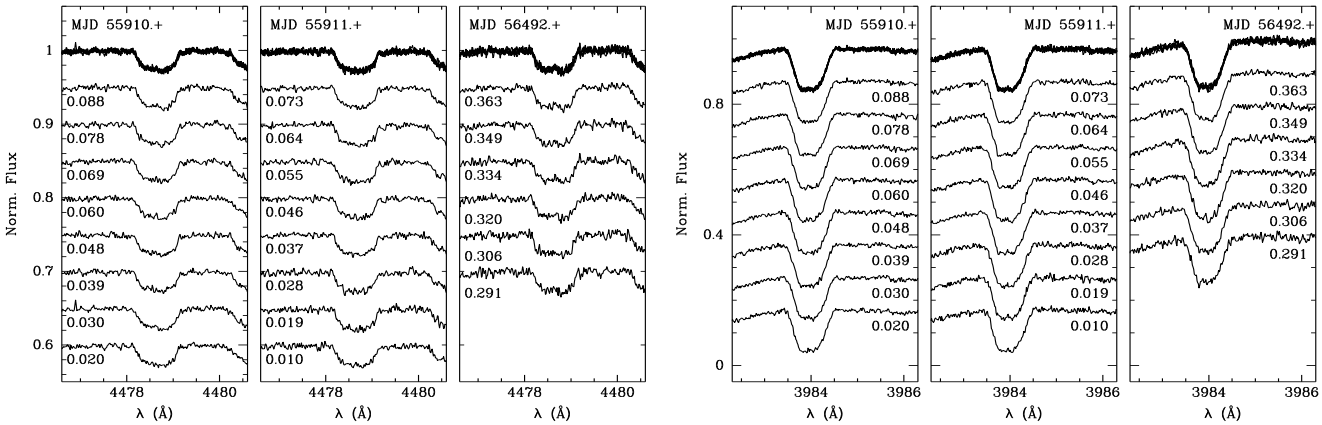

Figure 10. The behaviour of the line profiles of the Mn II λ4478 line (left panel) and the Hg II λ3984 line (right panel) in HARPSpol subexposures obtained on 2011 December 15 and 16, and on 2013 July 19. The overplotted profiles are presented on the top.

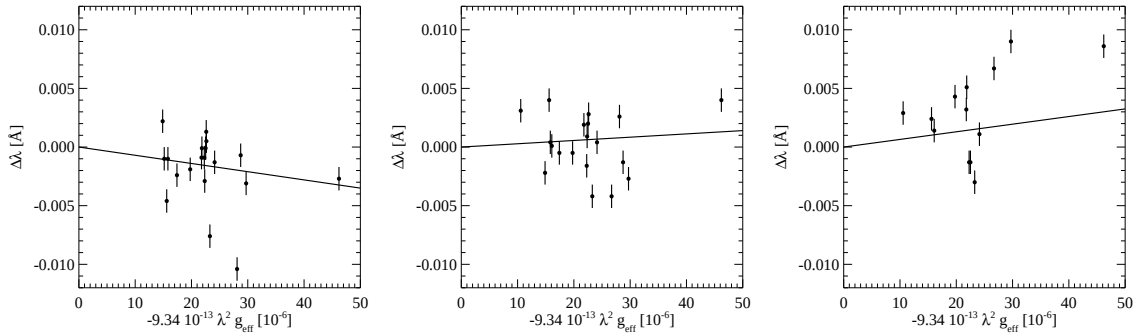

Figure 11. Linear regression analysis applied to the observations on three different nights. For each line, the shift between the line centres of gravity in the right and left circularly polarised spectra is plotted against $-9.34\ 10^{-13}\lambda^2 g_{\rm eff}$. The straight lines represent the best fit resulting from a linear regression analysis.

lines. The quality of the selection varies strongly from star to star, depending on binarity, line broadening, and the richness of the spectrum. The best 22, mostly blend-free, Mn II lines, including also six Mn II lines used in the abundance determination, we employed in the diagnosis of the magnetic field on the surface of HD 19400 are presented in Table 5 together with their Landé factors. The Landé factors were taken from Kurucz's list of atomic data[5]. As a first step, we used for the measurements the moment technique developed by Mathys (e.g. Mathys 1991). This technique allows us not only the determination of the mean longitudinal magnetic field, but also to prove the presence of crossover effect and quadratic magnetic fields. For each line, the measured shifts between the line profiles in the left- and right-hand circularly polarised HARPS spectra are presented in Table 5. The linear regression analysis in the $\Delta\lambda$ versus $\lambda^2 g_{\rm eff}$ diagram, following the formalism discussed by Mathys (1991, 1994), yields values for the mean longitudinal magnetic field $\langle B_{\rm z}\rangle$ between -70 G and $+65$ G. A weak negative longitudinal magnetic field $\langle B_z\rangle = -70 \pm 23$ G at 3σ level is measured on the first epoch, and $\langle B_z\rangle = 65 \pm 30$ G at 2.2σ level on the third epoch.

Table 6. Magnetic field measurements of HD 19400 using HARPS. In the first column, we list the modified Julian date of mid-exposure followed by the measurements of the mean longitudinal magnetic field using Mn II lines from polarised spectra and null polarisation spectra. All quoted errors are 1σ uncertainties.

MJD	$\langle B_{\rm z}\rangle_{\rm Mn}$ [G]	$\langle B_{\rm z}\rangle_{\rm Mn,N}$ [G]
55910.054	−70±23	−13±24
55911.042	28±18	−18±21
56492.327	65±30	25±32

Further, the mean longitudinal magnetic fields $\langle B_{\rm z}\rangle_{\rm Mn,N}$ were measured from null polarisation spectra, which are calculated by combining the subexposures in such a way that polarisation cancels out. The results of our measurements are presented in Table 6, and the corresponding linear regression plots are shown in Fig. 11. The measurements on the spectral lines of Mn II using null spectra are labeled by

[5] http://kurucz.cfa.harvard.edu/atoms

N in Table 6. Since no significant fields could be determined from null spectra, we conclude that any noticeable spurious polarisation is absent. No significant crossover and mean quadratic magnetic field have been detected on the three observing epochs.

Our assumption that the inhomogeneous distribution of Mn II over the stellar surface is due to the action of a magnetic field does not exclude the possibility that also ions with less pronounced line profile variability are inhomogeneously distributed across the stellar surface. Indeed, they could be concentrated towards the rotation poles, or have a predominantly symmetric distribution about the rotation axis. Among the elements showing less pronounced line profile variations in the spectra, the most numerous lines belong to Fe II and P II. Additional magnetic field measurements have been thus carried out using 35 Fe II and 33 P II lines listed in Table A1. Neither measurements using the Fe II lines nor the P II lines showed evidence for the presence of a magnetic field.

During the last few years, a number of attempts to detect mean longitudinal magnetic fields in HgMn stars have been made by several authors using the line addition technique, the least-squares deconvolution (LSD; e.g. Makaganiuk et al. 2011a,b), and the multi-line Singular Value Decomposition (SVD) technique (Hubrig et al. 2014). A high level of precision, from a few to tens of Gauss, is achieved through application of these techniques (Donati et al. 1997; Carroll et al. 2012), which combine hundreds of spectral lines of various elements. In such techniques an assumption is made that all spectral lines are identical in shape and can be described by a scaled mean profile. However, the lines of different elements with different abundance distributions across the stellar surface sample the magnetic field in different manners. Combining them, as is done with such techniques, may lead to the dilution of the magnetic signal or even to its (partial) cancellation, if enhancements of different elements occur in regions of opposite magnetic polarities. A shortcoming of both techniques is that a high level of precision is achievable only if a large number of lines is involved in the analysis.

In Fig. 12, we present the results of the SVD analysis of the observations on all three epochs using 32 Mn II lines selected from the VALD database (e.g., Piskunov et al. 1995; Kupka et al. 2000). We note that although the S/N of the two datasets obtained in 2011 is higher than for the most recent observation, the reconstruction for the last observation was performed with a smaller number of Eigenprofiles, which results in a smaller relative noise contribution. As the noise level scales with the effective dimension of the signal subspace (see Sect. 3 of Carroll et al. 2012), the noise levels of the reconstructed profiles for all three nights are approximately the same. On the first epoch, the measurement using the SVD technique shows the longitudinal magnetic field $\langle B_z \rangle = -76 \pm 25$ G. Using the false alarm probability (FAP; Donati et al. 1992) in the region of the whole Stokes I line profile, we obtain for this measurement $FAP = 0.008$. According to Donati et al. (1992), an FAP smaller than 10^{-5} can be considered as definite detection, while $10^{-5} < FAP < 10^{-3}$ are considered as marginal detections. We note that at this epoch the Zeeman feature is well visible in the Stokes V spectrum. However, the obtained FAP value is too high for a marginal detection. The interesting fact is that the observed Stokes V Zeeman feature is slightly shifted to the blue from the line center.

For the second epoch, we measure the mean longitudinal magnetic field $\langle B_z \rangle = 9 \pm 35$ G with the corresponding FAP value of 0.045. The observed Zeeman feature in the SVD Stokes V profile is reminiscent of a typical crossover profile, and, similar to the Zeeman feature in the first epoch, is also slightly shifted to the blue from the line center. The corresponding FAP values are 0.045 for the second epoch and 0.25 for the third epoch. Especially intriguing is the appearance of the SVD Stokes I profile with the corresponding Zeeman feature in the SVD Stokes V profile obtained for the third epoch. The shape of the SVD Stokes I profile shows a slight splitting shifted from the line center, indicating that we likely observe in this phase two Mn surface spots. If we assume that the Zeeman feature in the SVD Stokes V profile is not due to pure noise, then the observed negative and positive peaks in the Zeeman feature could probably correspond to two different Mn spots. The measured field for these features indicates a magnetic field of about -35 G for the negative peak and $+35$ G for the positive peak with $FAP = 0.029$. On the other hand, it is clear that the amplitude of the features inside the SVD profiles is comparable to the amplitude of the noise outside the SVD profiles.

A similar analysis using the SVD technique was carried out for 115 Fe II and 33 P II lines selected from the VALD database. The measurement on the first epoch using Fe II shows a longitudinal magnetic field $\langle B_z \rangle = -91 \pm 35$ G with a false alarm probability $FAP = 0.003$. For the second epoch, we obtained $\langle B_z \rangle = -28 \pm 21$ G with $FAP = 0.009$. No indications for a probable presence of a weak magnetic field was found on the third epoch. The obtained FAP value for the measurement on the first epoch is lower than that obtained for the measurement on the Mn II lines, but is still three times too high for a marginal detection.

No field detection was achieved in the analysis using the P II lines, where the Stokes V spectra appear rather flat on all three epochs. In Figs. 13 and 14, we present the results of the SVD analysis using the Fe II and P II lines, respectively.

In summary, although some indications on the probable existence of a weak magnetic field in HD 19400 are found in our analysis, no definite conclusion on the presence of the magnetic field and its topology can currently be drawn. Obviously, more high-resolution, high S/N polarimetric observations are urgently needed to properly understand the nature of this type of stars.

6 DISCUSSION

In this work, we used high quality HARPSpol spectra of the PGa star HD 19400 to carry out an abundance analysis, search for spectral variability, and the presence of a weak magnetic field. We present the abundances of various elements determined using an ATLAS12 model, including the abundances of a number of elements not analysed by previous studies. We also report on the first detection of anomalous shapes of line profiles belonging to Mn and Hg. We suggest that the variability of the line profiles of certain elements is caused by a non-uniform surface distribution of these elements similar to the presence of chemical spots detected in HgMn stars.

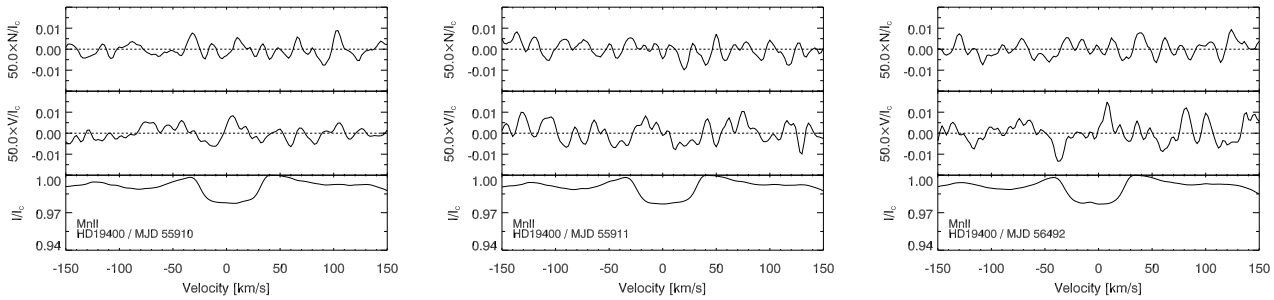

Figure 12. From left to right, we present the Mn II SVD profiles of HD 19400 obtained at the three different epochs from polarised spectra and null polarisation spectra. From bottom to top, one can see the I, V, and N profiles. The V and N profiles were expanded by a factor of 50 for better visibility.

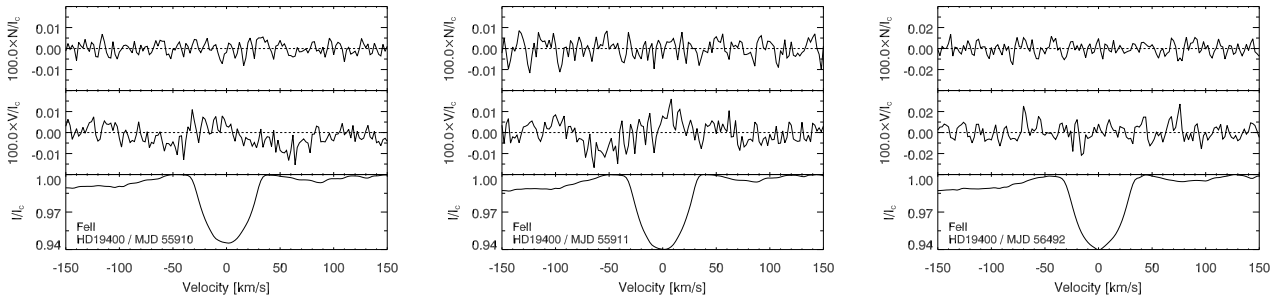

Figure 13. From left to right, we present the Fe II SVD profiles of HD 19400 obtained at the three different epochs from polarised spectra and null polarisation spectra. From bottom to top, one can see the I, V, and N profiles. The V and N profiles were expanded by a factor of 100 for better visibility.

One important task for future studies is to obtain detailed information on the pulsation behaviour of spectral lines in a few PGa stars by monitoring the behaviour of line profiles based on high quality spectroscopic time series over several hours using short exposures of the order of minutes. Current stellar models do not predict nonradial pulsations of the order of 5–20 min in mid B-type stars similar to those detected in roAp stars. On the other hand, such pulsations were not originally predicted for roAp stars either. In roAp stars, the pulsation variability is best detected in the line profiles of doubly ionised rare earth elements that build element clouds in high atmospheric layers. In close parallel to roAp stars, a theoretical consideration of B-type stars with Hg and Mn overabundances suggest that these elements can be concentrated in high-altitude clouds (above $\log \tau = -4$; e.g., Michaud et al. 1974; Alecian et al. 2011), with a potential effect of weak magnetic fields on their formation (e.g. Alecian 2013). Clearly, a careful investigation of the variability of mid B-type stars is of great interest to studies of stellar structure and evolution.

Our measurements of the magnetic field with the moment technique using 22 Mn II lines indicate the potential presence of a weak variable longitudinal magnetic field of the order of tens of gauss. The question of the presence of weak magnetic fields in stars with Hg and Mn overabundances is still under debate. Bagnulo et al. (2012) used the ESO FORS 1 pipeline to reduce the full content of the FORS 1 archive, among them one polarimetric observation of HD 19400 at MJD = 52852.371. While Hubrig et al. (2006b) reported for this epoch a mean longitudinal magnetic field $\langle B_z \rangle_{\rm all} = 151 \pm 46$ G measured using the whole spectrum and a longitudinal magnetic field $\langle B_z \rangle_{\rm hyd} = 217 \pm 65$ G using only the hydrogen lines, Bagnulo et al. (2012) measured $\langle B_z \rangle_{\rm all} = 124 \pm 85$ G, i.e. a field at a significance level of only 1.5σ. The authors state that very small instrument flexures, negligible in most of the instrument applications, may be responsible for some spurious magnetic field detections.

Our results using high-resolution spectropolarimetry are indicative of the potential presence of a weak magnetic field in HD 19400. Applying the moment technique to Mn lines, we measure a weak negative longitudinal magnetic field $\langle B_z \rangle = -70 \pm 23$ G at 3σ level on the first epoch. At the same epoch the results from the SVD analysis of the observations using Mn II lines show the longitudinal magnetic field $\langle B_z \rangle = -76 \pm 25$ G, and for the SVD analysis of Fe II lines we obtain $\langle B_z \rangle = -91 \pm 35$ G. However, the obtained FAP values, 0.008 and 0.003, are above the value 10^{-3}, and thus too high for a marginal detection according to Donati et al. (1992). We note that the presented work is based on spectra obtained only at three different nights. To get a better insight into the nature of PGa stars, it is important to carry out a more complete study based on spectropolarimetric monitoring over the rotation period.

ACKNOWLEDGMENTS

We thank the referee Gautier Mathys for his useful comments. Based on observations made with ESO telescopes at the La Silla Paranal Observatory under programme IDs 71.D-0308(A) and 091.D-0759(A), and data obtained from

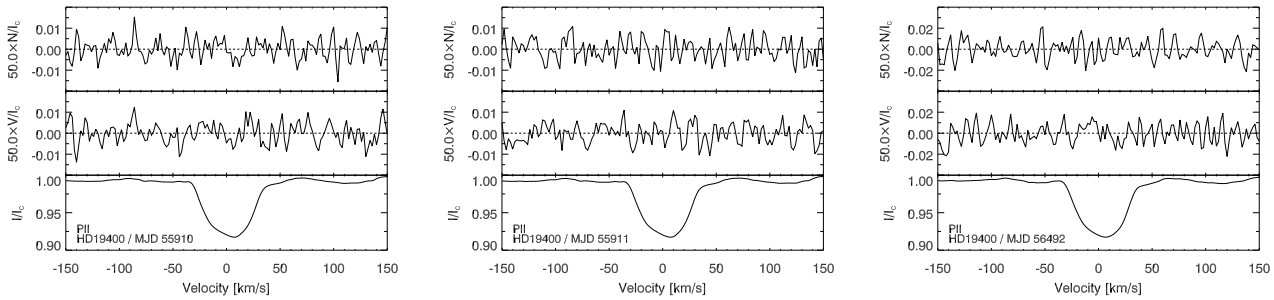

Figure 14. From left to right, we present the P II SVD profiles of HD 19400 obtained at the three different epochs from polarised spectra and null polarisation spectra. From bottom to top, one can see the I, V, and N profiles. The V and N profiles were expanded by a factor of 50 for better visibility.

the ESO Science Archive Facility under request number MSCHOELLER51580. This work has made use of the VALD database, operated at Uppsala University, the Institute of Astronomy RAS in Moscow, and the University of Vienna.

REFERENCES

Alecian G., 2013, EAS Publ. Ser., 63, 219
Alecian G., Artru M.-C., 1987, A&A, 186, 223
Alecian G., Stift M. J., Dorfi E. A., 2011, MNRAS, 418, 986
Alonso M. S., Lopez-Garcia Z., Malaroda S., Leone F., 2003, A&A, 402, 331
Artru M.-C., Freire-Ferrero R., 1988, A&A, 203, 111
Asplund, M., Grevesse, N., Sauval, A.J., Scott, P. 2009, Annual Review of Astronomy and Astrophysics 47, 481
Bagnulo S., Landstreet J. D., Fossati L., Kochukhov O., 2012, A&A, 538, 129
Bilir S., Karaali S., Ak S., Yaz E., Cabrera-Lavers A., Coşkunoğlu K. B., 2008, MNRAS, 390, 1569
Briquet M., Korhonen H., González J. F., Hubrig S., Hackman T., 2010, A&A, 511, A71
Carroll T. A., Strassmeier K. G., Rice J. B., Künstler A., 2012, A&A, 548, A95
Castelli F., Hubrig S., 2004, A&A, 425, 263
Castelli F., Hubrig S., 2007, A&A, 475, 1041
Castelli F., Kurucz R. L., 2003, in Piskunov N., Weiss W. W., Gray D. F., eds, Proc. IAU Symp. 210, Modelling of Stellar Atmospheres, p. 20P
Castelli F., Kurucz R. L., 2006, A&A, 454, 333
Castelli F., Kurucz R. L., 2010, A&A, 520, A57
Collado A. E., Lopez-Garcia Z., 2009, RMxAA, 45, 95
Díaz C. G., González J. F., Levato H., Grosso M., 2011, A&A, 531, A143
Dommanget J., Nys O., 2002, Catalogue of the Components of Double and Multiple Stars (CCDM), Observations et Travaux, 54, 5
Donati J.-F., Semel M., Rees D. E., 1992, A&A, 265, 669
Donati J.-F., Semel M., Carter B. D., Rees D. E., Collier Cameron A., 1997, MNRAS, 291, 658
Drake N. A., Hubrig S., Schöller M., Ilyin I., Castelli F., Pereira C. B., Gonzalez J. F., 2013, preprint (arXiv:1309.5501)
Fuhr J. R., Wiese W. L., 2006, Journal of Physical and Chemical Reference Data, 35, 1669
Hauck B., Mermilliod M., 1998, A&AS, 129, 431
Hubrig S., Mathys G., 1995, Comm. on Astroph., 18, 167
Hubrig S., González J. F., Savanov I., Schöller M., Ageorges N., Cowley C. R., Wolff, B., 2006a, MNRAS, 371, 1953
Hubrig S., North P., Schöller M., Mathys G., 2006b, Astron. Nach., 327, 289
Hubrig S., et al., 2010, MNRAS, 408, L61
Hubrig S., et al., 2011, Astron. Nach., 332, 998
Hubrig S., et al., 2012, A&A, 547, A90
Hubrig S., et al., 2014, MNRAS, 440, L6
Ilyin I., 2012, Astron. Nach., 333, 213
Kling R., Schnabel R., Griesmann U., 2001, ApJS, 134, 173
Korhonen H., et al., 2013, A&A, 553, A27
Kupka F. G., Ryabchikova T. A., Piskunov N. E., Stempels H. C., Weiss W. W., 2000, Baltic Astronomy, 9, 590
Kurucz R. L., 2005, Memorie della Societa Astronomica Italiana Supplementi, 8, 14
Kurucz R. L., 2011, Canadian Journal of Physics, 89, 417
Maitzen H. M., 1984, A&A, 138, 493
Makaganiuk V., et al., 2011a, A&A, 529, A160
Makaganiuk V., et al., 2011b, A&A, 525, A97
Mathys G., 1991, A&AS, 89, 121
Mathys G., 1994, A&AS, 108, 547
Michaud G., Reeves H., Charland Y., 1974, A&A, 37, 31
Miglio A., Montalbán J., Dupret M.-A., 2007, Comm. in Asteroseismology, 151, 48
Moon T. T., 1985, Commun. Univ. London Obs., 78
Nielsen K., Karlsson H., Wahlgren G. M., 2000, A&A, 363, 815
Piskunov N. E., et al. 1995, A&AS, 112, 525
Rachkovskaya T. M., Lyubimkov L. S., Rostopchin S. I., 2006, Astronomy Reports, 50, 123
Ryabchikova T. A., Smirnov Y. M., 1994, Astronomy Reports, 38, 70
Sadakane K., et al., 2001, PASJ, 53, 1223
Schlegel D. J., Finkbeiner D. P., Davis M., 1998, ApJ, 500, 525
Scuflaire R., Théado S., Montalbán J., Miglio A., Bourge P.-O., Godart M., Thoul A., Noels A., 2008, Ap&SS, 316, 83
Sigut T. A. A., Landstreet J. D., 1990, MNRAS, 247, 611
Sigut T. A. A., Landstreet J. D., Shorlin, S. L. S., 2000, ApJ 530, L89
Sigut T. A. A., A&A, 377, L27
Snik F., Jeffers S., Keller C., Piskunov N., Kochukhov O., Valenti J., Johns-Krull C., 2008, in Society of Photo-

Optical Instrumentation Engineers (SPIE) Conf. Ser., 7014, E22
van Leeuwen F., 2007, A&A, 474, 653
Wahlgren, G. M., Hubrig, S., 2000, A&A, 362, L13
Wahlgren, G. M., Hubrig, S., 2004, A&A 418, 1073
Yüce K., Castelli F., Hubrig S., 2011, A&A, 528, A37

APPENDIX A: LINE LISTS AND ABUNDANCES

In Table A1 we list all lines used in our abundance analysis.

Table A1. Line by line abundances of HD 19400 from the ATLAS12 model with parameters $T_{\rm eff} = 13\,500$ K, log $g = 3.9$. In the second and third columns, we give the oscillator strength with the corresponding data base source. The low excitation potential is listed in column 4, followed by the equivalent width and the derived abundance. For a number of lines, the abundance was derived from line profiles.

HD 19400[13500,3.9,ATLAS12]						
λ(Å)	log gf	Ref.[a]	$\chi_{\rm low}$	W(mÅ)	log($N_{\rm elem}/N_{\rm tot}$)	Remarks
log(N(He I)/$N_{\rm tot}$) = -2.17 ± 0.08:						
3867.4723	−2.038	NIST5	169086.766	profile	−2.155	
3867.4837	−2.260	NIST5	169086.843	profile	−2.155	
3867.6315	−2.737	NIST5	169087.631	profile	−2.155	
4009.2565	−1.447	NIST5	171134.897	profile	−2.155	
4026.1844	−2.628	NIST5	169086.766	profile	−2.155::	no fit
4026.1859	−1.453	NIST5	169086.766	profile	−2.155::	
4026.1860	−0.704	NIST5	169086.766	profile	−2.155::	
4026.1968	−1.453	NIST5	169086.843	profile	−2.155::	
4026.1983	−0.976	NIST5	169086.843	profile	−2.155::	
4026.3570	−1.328	NIST5	169087.831	profile	−2.155::	
4120.8108	−1.723	NIST5	169086.766	profile	−2.155	
4120.8237	−1.945	NIST5	169086.843	profile	−2.155	
4120.9916	−2.422	NIST5	169087.831	profile	−2.155	
4143.7590	−1.201	NIST5	171134.897	profile	−2.155	
4387.9291	−0.887	NIST5	171134.897	profile	−2.155:	no fit in red wing
4437.5534	−2.015	NIST5	171134.897	profile	−2.00	
4471.4704	−2.211	NIST5	169086.766	profile	−2.155	no fit in the core
4471.4741	−1.036	NIST5	169086.766	profile	−2.155	
4471.4743	−0.287	NIST5	169086.766	profile	−2.155	
4471.4856	−1.035	NIST5	169086.843	profile	−2.155	
4471.4893	−0.558	NIST5	169086.843	profile	−2.155	
4471.6832	−0.910	NIST5	169087.831	profile	−2.155	
4713.1382	−1.276	NIST5	169086.766	profile	−2.155	
4713.1561	−1.499	NIST5	169086.483	profile	−2.155	
4713.3757	−1.976	NIST5	169087.831	profile	−2.155	
4921.9310	−0.443	NIST5	171134.897	profile	−2.301	no fit in red wing
5015.6780	−0.820	NIST5	166277.440	profile	−2.155	
5047.7385	−1.587	NIST5	171134.897	profile	−2.155	
5875.5987	−1.516	NIST5	169086.766	profile	−2.301	
5875.6139	−0.339	NIST5	169086.766	profile	−2.301	
5875.6148	+0.409	NIST5	169086.766	profile	−2.301	
5875.6251	−0.339	NIST5	169086.843	profile	−2.301	
5875.6403	+0.138	NIST5	169086.843	profile	−2.301	
5875.9663	−0.214	NIST5	169087.831	profile	−2.301	
6678.1517	+0.329	NIST5	171134.897	profile	−2.301	
log(N(C II)/$N_{\rm tot}$) = -4.12 ± 0.02						
3918.968	−0.533	NIST5	131724.37	profile	−4.1	blend
4267.001	+0.563	NIST5	145549.27	profile	−4.1	blend
4267.261	+0.716	NIST5	145550.70	profile	−4.1	
4267.261	−0.584	NIST5	145550.70	profile	−4.1	
6578.052	−0.021	NIST5	116537.65	profile	−4.15	
log(N(O I)/$N_{\rm tot}$) = −3.9						
6155.971	−1.011	NIST5	86625.757	profile	−3.9	
6155.989	−1.120	NIST5	86625.757	profile	−3.9	
6156.755	−0.899	NIST5	86627.778	profile	−3.9	
6156.778	−0.694	NIST5	86627.778	profile	−3.9	

Table A1. Continued.

HD 19400[13500,3.9,ATLAS12]						
λ(Å)	log gf	Ref.[a]	$\chi_{\rm low}$	W(mÅ)	log($N_{\rm elem}/N_{\rm tot}$)	Remarks
log(N(Ne I)/$N_{\rm tot}$) = −3.77 ± 0.07						
5852.488	−0.455	NIST5	135888.717	14.1	−3.79	
6096.163	−0.297	NIST5	134458.287	17.7	−3.85	
6143.063	−0.098	NIST5	134041.840	20.9	−3.86	
6266.495	−0.357	NIST5	134810.740	19.6	−3.68	
6402.248	+0.345	NIST5	134041.840	36.7	−3.72	
6717.043	−0.356	NIST5	135888.717	15.3	−3.70	
log(N(Na I)/$N_{\rm tot}$) = −5.71						
5889.950	+0.108	NIST5	0.00	profile	−5.71	blend
5895.924	−0.194	NIST5	0.00	profile	−5.71	blend
log(N(Mg II)/$N_{\rm tot}$) = −5.06						
4390.572	−0.523	NIST5	80650.020	profile	−5.06	blend
4390.514	−1.478	NIST5	80650.020	profile	−5.06	blend
4427.994	−1.208	NIST5	80619.500	profile	−5.06	blend
4481.126	+0.749	NIST5	71490.190	profile	−5.06	blend
4481.150	−0.553	NIST5	71490.190	profile	−5.06	blend
4481.325	+0.594	NIST5	71491.063	profile	−5.06	blend
log(N(Al II)/$N_{\rm tot}$) ⩽ −6.77						
4663.046	−0.290	NIST5	85481.35	not obs	⩽−6.77	blend
5593.300	+0.410	NIST5	106920.56	not obs	⩽−6.77	blend
log(N(Si II)/$N_{\rm tot}$) = −4.36 ± 0.17						
3856.018	−0.406	NIST5	55325.18	123.7	−4.63	
3862.595	−0.757	NIST5	55309.35	114.7	−4.42	
4075.452	−1.400	NIST5	79355.02	22.6	−4.48	
5688.817	+0.126	NIST5	114414.58	12.4	−4.40	blend telluric
5701.37	−0.057	NIST5	114327.15	8.7	−4.42	blend telluric
5978.93	+0.084	NIST5	81251.32	71.0	−4.52	
6347.109	+0.149	NIST5	65500.47	164.7	−4.28	
6371.371	−0.082	NIST5	65500.47	131.3	−4.34	
6660.532	+0.162	NIST5	116978.38	15.5	−4.06	
6671.840	+0.409	NIST5	117178.06	19.7	−4.09	
log(N(Si III)/$N_{\rm tot}$) = −4.37 ± 0.02						
4552.622	+0.292	NIST5	153377.050	16.7	−4.39	
4567.840	+0.068	NIST5	153377.050	13.4	−4.35	

Table A1. Continued.

HD 19400[13500,3.9,ATLAS12]						
λ(Å)	log gf	Ref.[a]	$\chi_{\rm low}$	W(mÅ)	log($N_{\rm elem}/N_{\rm tot}$)	Remarks
log(N(P II)/$N_{\rm tot}$) = −4.26 ± 0.15						
4044.576	+0.669	K12	107360.25	68.5	−4.43	
4420.717	−0.330	NIST5	88893.22	52.9	−4.40	
4452.472	−0.083	K12	105302.37	34.0	−4.30	
4463.027	+0.164	K12	105549.67	38.2	−4.46	
4466.140	−0.560	NIST5	105549.67	21.1	−4.20	reversal ?
4475.270	+0.440	NIST5	105549.67	48.0	−4.51	
4499.230	+0.470	NIST5	107922.93	58.0	−4.16	
4530.823	+0.074	K12N	105302.37	37.0	−4.40	
4554.854	−0.084	K12	106001.25	33.9	−4.20	
4565.287	−0.520	NIST5	106001.25	20.9	−4.23	
4581.716	−1.121	K12	101635.69	15.5	−4.01	
4589.846	+0.400	NIST5	103165.61	55.2	−4.30	
4602.069	+0.740	NIST5	103667.86	62.7	−4.44	
4626.708	−0.320	NIST5	103339.14	29.8	−4.23	
4658.309	−0.320	NIST5	103667.86	21.0	−4.49	asymm ?, uncertain laboratory wavelength?
4679.028	−0.319	K12N	106001.25	19.3	−4.45	
4927.197	−0.799	K12N	103165.61	12.5	−4.33	
4935.631	−0.161	NIST5	111507.66	17.6	−4.37	
4943.497	+0.060	NIST5	103667.86	39.2	−4.27	
5344.729	−0.280	K12N	86597.55	55.4	−4.15	
5409.722	−0.390	NIST5	86743.96	60.5	−4.14	
5425.880	+0.288	K12N	87124.60	103.7	−4.08	
5499.697	−0.441	K12N	87124.60	49.1	−4.30	
5541.139	−0.515	K12N	105302.37	16.8	−4.23	
6024.178	+0.198	K12N	86743.96	106.5	−3.84	
6034.039	−0.151	K12N	86597.55	73.5	−4.00	
6043.084	+0.416	NIST5	87124.60	103.4	−4.07	
6055.504	+0.056	NIST5	107922.93	23.9	−4.27	
6087.837	−0.346	NIST5	86743.96	56.7	−4.13	
6165.600	−0.341	NIST5	87124.60	49.8	−4.25	
6232.297	−1.652	K12N	87124.60	7.8	−4.35	
6435.282	−1.043	K12	87804.10	21.2	−4.24	
6713.283	−1.257	K12	86743.96	18.8	−4.21	
log(N(P III)/$N_{\rm tot}$) = −4.44 ± 0.09						
4059.312	−0.236	K13Ph	116885.87	22.5	−4.58	
4080.089	−0.494	K13Ph	116874.56	21.9	−4.35	
4222.198	+0.218	K13Ph	117835.95	30.8	−4.44	
4246.720	−0.120	NIST5	117835.95	23.3	−4.40	
log(N(S II)/$N_{\rm tot}$) = −5.82						
4162.665	+0.777	NIST5	128559.160	6.2	−5.82	
log(N(Ca II)/$N_{\rm tot}$) = −5.50:						
3933.663	+0.135	NIST5	0.000	profile	−5.50:	

Table A1. Continued.

HD 19400[13500,3.9,ATLAS12]						
λ(Å)	log gf	Ref.[a]	$\chi_{\rm low}$	W(mÅ)	log($N_{\rm elem}/N_{\rm tot}$)	Remarks
log(N(Ti II)/$N_{\rm tot}$) = -6.35 ± 0.07						
4163.644	−0.130	NIST5	20891.660	24.4	−6.28	
4290.215	−0.850	NIST5	9395.710	18.8	−6.36	
4294.094	−0.930	NIST5	8744.250	19.6	−6.29	
4300.042	−0.442	NIST5	9518.060	31.5	−6.40	
4399.765	−1.190	NIST5	9975.920	11.4	−6.27	
4443.801	−0.717	NIST5	8710.440	27.1	−6.28	
4501.270	−0.767	NIST5	8997.710	21.2	−6.38	
4563.757	−0.690	NIST5	9850.900	18.2	−6.51	
4571.971	−0.317	NIST5	12676.970	30.6	−6.37	
log(N(Cr II)/$N_{\rm tot}$) = -6.24 ± 0.09						
4592.049	−1.217	NIST5	32854.950	9.4	−6.21	
4616.629	−1.291	NIST5	32844.760	5.9	−6.36	
4618.803	−0.860	SL	32854.950	10.7	−6.25	
4634.070	−0.990	SL	32844.760	8.1	−6.26	
4824.127	−0.980	SL	31219.350	13.6	−6.10	
log(N(Mn II)/$N_{\rm tot}$) = -4.94 ± 0.18						
4206.367	−1.553	KSG	43258.640	30.4	−4.78	hfs, weak reversal
4292.237	−1.544	KSG	43394.439	23.6	−4.99	hfs, flat core
4363.255	−2.094	K11	44899.820	15.8	−4.61	hfs, bad continuum
4365.217	−1.328	K11	53017.160	11.6	−5.12	hfs, reversal
4478.637	−0.935	K11	53597.130	21.9	−5.09	hfs, reversal
4518.956	−1.322	K11	53597.130	13.0	−5.03	
log(N(Fe II)/$N_{\rm tot}$) = -3.80 ± 0.14						
4122.659	−3.300	FW06	20830.553	36.4	−3.73	
4258.148	−3.480	FW06	21812.045	29.9	−3.68	
4273.320	−3.300	FW06	21812.045	29.7	−3.86	
4286.271	−1.578	K13Fe	62171.624	18.6	−3.76	
4296.566	−2.930	FW06	21812.045	45.4	−3.78	
4303.170	−2.610	FW06	21812.045	60.6	−3.63	
4369.400	−3.580	FW06	22409.818	24.5	−3.70	
4416.819	−2.600	FW06	22409.818	51.3	−3.91	
4449.611	−1.678	K13Fe	63948.803	10.3	−3.99	
4489.176	−2.970	FW06	22810.346	39.9	−3.85	
4491.397	−2.640	FW06	23031.283	47.9	−3.93	
4507.091	−1.909	K13Fe	62689.874	11.9	−3.65	
4508.280	−2.350	FW06	23031.283	62.9	−3.76	
4515.333	−2.360	FW06	22939.351	65.3	−3.61	
4520.218	−2.620	FW06	22637.195	52.9	−3.82	
4522.628	−1.990	FW06	22939.351	69.6	−3.92	
4541.516	−2.970	FW06	23031.283	43.3	−3.74	
4555.887	−2.250	FW06	22810.346	63.5	−3.84	
4576.333	−2.920	FW06	22939.351	40.5	−3.88	
4582.830	−3.062	FW06	22939.351	34.5	−3.90	
4583.829	−1.940	FW06	22637.195	85.7	−3.55	
4620.513	−3.190	FW06	22810.346	22.9	−4.11	

Table A1. Continued.

HD 19400[13500,3.9,ATLAS12]						
λ(Å)	log gf	Ref.[a]	$\chi_{\rm low}$	W(mÅ)	log($N_{\rm elem}/N_{\rm tot}$)	Remarks
log(N(Fe II)/$N_{\rm tot}$) = −3.80 ± 0.14 (cont.)						
4629.331	−2.257	FW06	22637.195	64.6	−3.81	
4635.316	−1.476	K13FeN	48039.090	46.1	−3.75	
4913.296	+0.016	J07	82978.717	37.4	−3.63	
4923.921	−1.206	FW06	23317.635	97.0	−3.97	
4993.350	−3.680	FW06	22637.195	20.2	−3.71	
5001.953	+0.933	J07	82853.704	70.2	−3.68	
5018.436	−1.350	FW06	23317.635	105.2	−3.67	
5030.632	+0.431	FW06	82978.717	45.5	−3.81	
5061.710	+0.204	K13Fe	83136.508	39.9	−3.72	
5169.028	−0.870	FW06	23317.635	104.3	−4.18	
5247.956	+0.550	FW06	84938.265	47.8	−3.70	
5493.831	+0.259	FW06	84685.245	33.5	−3.83	
5506.199	+0.923	J07	84863.382	60.1	−3.72	
log(N(Fe III)/$N_{\rm tot}$) = −3.82 ± 0.10						
4022.330	−2.040	K10	93392.300	9.3	−3.74	
4371.345	−3.026	K10	66464.800	9.5	−3.86	
4382.501	−2.980	K10	66523.020	12.4	−3.72	
4419.596	−2.207	K10	89084.790	23.3	−3.98	
log(N(Ni II)/$N_{\rm tot}$) = −5.84						
4067.031	−1.847	K10Ni	32499.530	20.9	−5.84	
log(N(Ga II)/$N_{\rm tot}$) = −5.19 ± 0.17						
4251.155	+0.350	RS94	113815.885	profile	−4.75	hfs, blend
4254.073	−0.230	RS94	113842.301	profile	−5.10	hfs
4255.720	+0.634	NKW	113842.301	profile	−5.25	hfs, blend
4255.936	−0.320	NKW	113842.301	profile	−5.25	
4261.488	−1.100	GUES	113883.193	profile	−5.15	hfs, blend
4262.014	+0.980	RS94	113883.193	profile	−5.15	hfs
4263.141	−0.500	GUES	113883.193	profile	−5.25	hfs
5219.658	+0.350	GUES	120550.431	profile	−5.20	blend
5338.240	+0.430	RS94	118429.967	profile	−5.40:	bad spectrum
5360.402	+0.420	RS94	118518.461	profile	−5.10	hfs, reversal ?
5363.585	+0.060	GUES	118518.461	profile	−5.30	hfs, blend
5416.318	+0.640	RS94	118727.870	profile	−5.20	hfs
5421.274	−0.050	NKW	118727.870	profile	−5.15	hfs
6334.07	+1.000	RS94	102944.595	profile	−5.40	hfs
6419.24	+0.570	RS94	102944.595	profile	−5.30	hfs
6455.92	−0.080	RS94	102944.595	profile	−5.30	hfs, blend
log(N(Sr II)/$N_{\rm tot}$) = −9.07						
4077.709	+0.148	NIST5	0.00	profile	−9.07	
log(N(Xe II)/$N_{\rm tot}$) = −4.65 ± 0.17						
4603.030	+0.018	NIST5	95064.38	29.1	−4.89	
4844.330	+0.491	NIST5	93068.44	48.4	−4.66	
5419.155	+0.215	NIST5	95064.38	37.8	−4.51	
6036.170	−0.609	NIST5	95396.74	17.8	−4.55	
6051.120	−0.252	NIST5	95437.67	26.0	−4.45	self-reversal ?
6097.570	−0.240	NIST5	95396.74	18.1	−4.88	

Table A1. Continued.

HD 19400[13500,3.9,ATLAS12]						
λ(Å)	log gf	Ref.[a]	$\chi_{\rm low}$	W(mÅ)	log($N_{\rm elem}/N_{\rm tot}$)	Remarks
$\log(N(\text{Hg II})/N_{\rm tot}) = -6.16 \pm 0.13$						
3983.931	−1.510	NIST5	35514.624	profile	−6.35	
5677.102	+0.820	NIST5	105544.042	12.6	−6.07	
6149.470	+0.150	NIST5	95714.406	profile	−6.07	blend

[a]: NIST5: NIST Atomic Spectra Database, version 5 at http://physics.nist.gov/pml/data/asd.cfm;
P II: K12: http://kurucz.harvard.edu/atoms/1501/gf1501.pos; K12N: the NIST5 log gf values are replaced by the K12 values;
P III: K13Ph: http://kurucz.harvard.edu/atoms/1502/gf1502.pos;
Cr II: SL: Sigut & Landstreet (1990);
Mn II: K11: Kurucz, R. L. 2011, private communication; KSG: Kling et al. (2001);
Fe II: FW06: Fuhr & Wiese (2006); J07: S. Johansson (2007), priv. comm.; K10: http://kurucz.harvard.edu/atoms/2602/gf2602.pos;
K13Fe: http://kurucz.harvard.edu/atoms/2601/gf2601.pos; K13FeN: the NIST5 log gf values are replaced by the K13Fe values;
Ni II: K10Ni: http://kurucz.harvard.edu/atoms/2801/gf2801.pos;
Ga II: NKW: Nielsen et al. (2000); RS94: Ryabchikova & Smirnov (1994); GUES: Guessed values on the basis of the line intensity.